JACS
JOURNAL OF THE AMERICAN CHEMICAL SOCIETY
pubs.acs.org/JACS
Article

Autonomous Nanoparticle Synthesis Guided by *In Situ* Multiscale Structural Characterization

Hyeong Jin Kim, Matthew R. Carbone, Fang Lu, Xiaohui Qu, Kristofer Reyes, Honghu Zhang, Lihua Zhang, Oleg Gang, and Yugang Zhang*,▽

Cite This: https://doi.org/10.1021/jacs.5c03875

Read Online

ACCESS | Metrics & More | Article Recommendations | Supporting Information

ABSTRACT: Autonomous synthesis platforms promise rapid exploration of vast parameter spaces; yet, integrating *in situ* structural characterization in closed-loop synthesis optimization remains challenging. We demonstrate a realization of such a closed-loop platform coupled with a droplet-flow microreactor, *in situ* X-ray scattering methods (SAXS/WAXS), and Gaussian process optimization to synthesize citrate-reduced Au nanoparticles with targeted characteristics. The system efficiently explored ∼19,000 synthesis recipes through 365 experiments, achieving precise control over size (4−60 nm) and polydispersity (σ < 0.11) across large citrate/gold ratios, exceeding traditional synthesis boundaries (1−10). Beyond confirming classical Turkevich−Frens trends, partial-dependence analysis revealed strong nonlinear coupling among precursor, citrate, and pH effects. Combining quantitative SAXS/WAXS analysis with electron microscopy characterization, we uncovered that crystallite size (d_c) and particle size (d) follow $d_c = 0.18d + \beta$, where synthesis chemistry controls the intercept β while maintaining a universal slope. This parallel-band structure enables independent tuning of crystallite domain size at fixed particle diameter through a combination of chloride, gold precursor, citrate, and pH contributions (cross-validated Spearman $\rho = 0.7 \pm 0.1$). High-resolution electron microscopy shows multiple lattice-fringe orientations within single particles, directly confirming polycrystalline domains and the ability to tune d_c at the fixed d. The platform's validation includes indistinguishable static versus flowing measurements, stable droplet transport at 100 °C, and <5% run-to-run variation, establishing a robust framework for mapping and controlling multiscale nanoparticle structure across expansive chemical spaces. The developed closed-loop platform can be applied to a borad range of nanosyntheis processes.

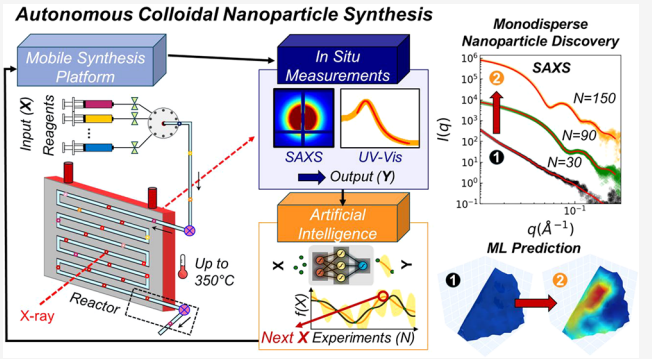

INTRODUCTION

Colloidal nanoparticles enable advances in catalysis, photonics, energy storage, and biomedicine.[1−5] Realizing their full potential requires precise control over key characteristics, such as size, uniformity, and crystallinity. Despite decades of research, control remains challenging due to complex formation pathways, coupled reaction-transport phenomena, and large parameter spaces.[6] Even six variables at ten levels imply one million combinations. Comprehensive mapping is essential both to discover robust synthesis protocols and to constrain mechanistic models of nanoparticle formation.[1,7,8]

Historically, nanoparticle synthesis has relied on empirical knowledge and iterative optimization with inherent limitations. For example, nanoparticle formation is highly sensitive to minor variations in reaction conditions, where small perturbations can substantially alter product features.[9−11] Moreover, incremental modifications of existing protocols often constrain innovation and limit comprehensive exploration of synthesis parameter spaces.[3,12,13] Recent advances in artificial intelligence (AI) and automated experimental platforms offer a path toward more systematic material discovery and optimization.[8,14−28] Autonomous systems integrating automated synthesis with machine-learning (ML)-guided decision-making represent a significant advance over traditional automation. While automation alone improves reproducibility and throughput,[29−31] machine learning captures complex, multivariate relationships between synthesis parameters and particle characteristics, enabling efficient exploration of high-dimensional parameter spaces.[14,20,32−36]

Current autonomous synthesis platforms face limitations in their ability to combine characterization approaches on multiple scales. While *in situ* characterization methods have advanced significantly, integrating such measurements directly

Received: March 4, 2025
Revised: November 26, 2025
Accepted: December 1, 2025

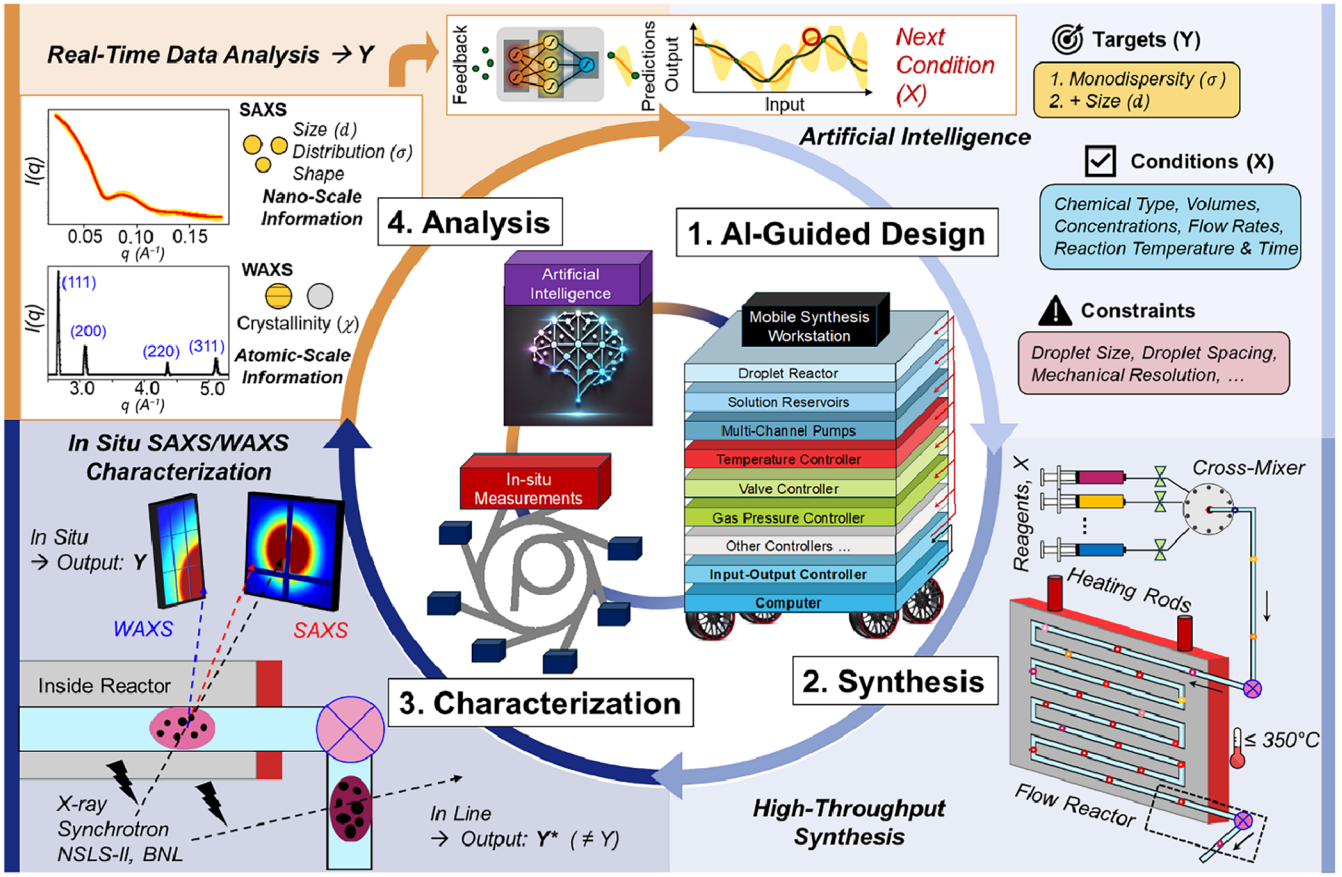

Figure 1. Closed-loop platform for autonomous colloidal nanoparticle synthesis. The system integrates (1) AI-guided experimental design: Gaussian process (GP) models map synthesis variables (X) to nanoparticle characteristics (Y) and propose informative next experiments via exploration/exploitation; (2) automated wet-chemistry on a mobile droplet-flow workstation; (3) *in situ* SAXS/WAXS at a synchrotron beamline to probe structure in the native reaction environment; and (4) real-time analysis extracting multiscale features (size d, polydispersity σ, crystallinity, χ). This closed-loop process enables exploration of synthesis parameter spaces beyond traditional boundaries, accessing regimes inaccessible to conventional approaches.

within autonomous synthesis loops during active reaction remains challenging. As detailed in Table S1, many systems rely on postsynthesis or downstream characterization that requires sample extraction or transfer. The robotic and fluidic platforms are two powerful systems for the automated synthesis of colloidal nanoparticles. Due to the large operation hardware and fixed location of many robotic systems, they typically utilize optical methods such as ultraviolet−visible (UV−vis) spectroscopy,[37,38] which provides limited structural information. Integration with advanced characterization tools, such as synchrotron X-ray facilities, remains challenging.

Fluidic platforms[26,39−47] offer improved portability and have enabled important advances for *in situ* characterizations. Levenstein et al. employed inline powder XRD to monitor crystallization pathways in segmented flow,[44] while Jackson et al. developed self-optimizing flow reactors with real-time nanoparticle characterization.[45] Pioneering work in autonomous synthesis with synchrotron feedback includes Rakita et al., who used synchrotron X-ray absorption spectroscopy (XAS) feedback to control Cu redox states in real-time,[46] and Pithan et al., who implemented machine learning-based autonomous experiments with X-ray reflectivity (XRR) at synchrotron beamlines to optimize redox states and crystallization pathways.[47] These studies established critical foundations for integrating X-ray characterization with automated synthesis, leveraging synchrotron sources' high brilliance and fast acquisition rates.

Building on these foundations, we extend autonomous capabilities by performing small- and wide-angle X-ray scattering (SAXS/WAXS), powerful tools for in-solution multiscale structure analysis,[48] directly within the reaction zone during reaction, where nanoparticles are synthesized. This *in situ* capability enables the capture of transient intermediates of reaction products and allows for correlation of structural evolution with the actual chemical conditions. Our platform integrates a droplet-flow microreactor with synchrotron SAXS/WAXS and Gaussian process optimization (Figure 1), providing three key capabilities: (1) simultaneous SAXS/WAXS yielding multiscale structural information from atomic arrangements to particle morphology during reaction; (Figure 2A−C); (2) a temperature-controlled flow reactor with integrated X-ray probing enabling multiscale structural measurements within the reaction environment and with ability to track reaction kinetics without sample extraction; and (3) real-time structural analysis and machine-learning algorithms that correlate synthesis conditions with structural outcomes of reaction products to guide next step synthesis experiments toward targeted nanoparticle characteristics. Controls verify indistinguishable static versus flowing measurements, stable droplet transport at ∼100 °C, and < ∼5% run-to-run variation (Methods; Figures S1−S3).

https://doi.org/10.1021/jacs.5c03875
J. Am. Chem. Soc. XXXX, XXX, XXX−XXX

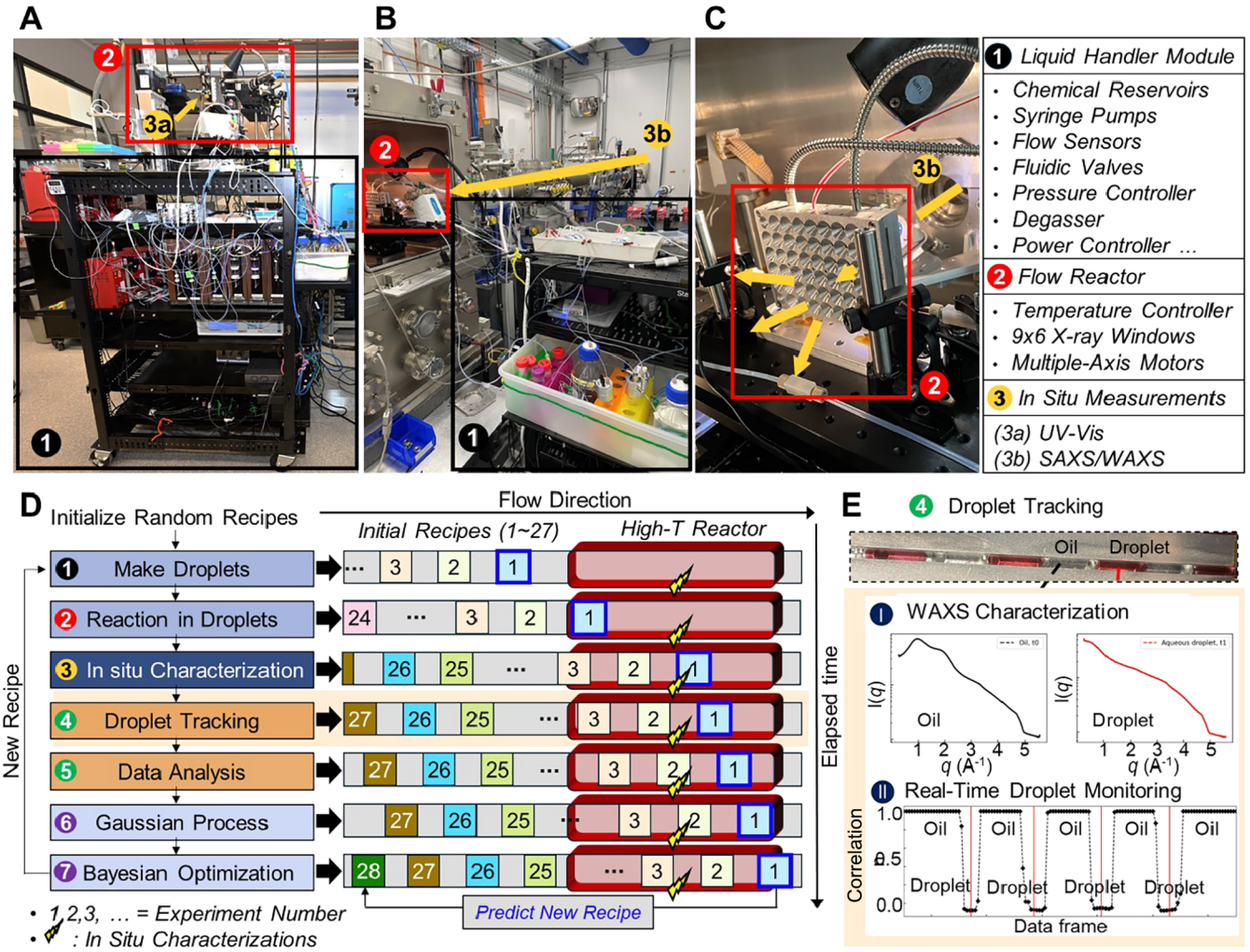

Figure 2. Implementation of real-time autonomous platform. (A) Mobile synthesis workstation integrates fluidics-based liquid handling, a droplet-flow reactor, *in situ* tools (X-ray and UV−Vis), and on-board data/ML modules. (B, C) Deployment at NSLS-II SMI (12-ID) with a temperature-controlled reactor and integrated X-ray windows for *in situ* SAXS/WAXS. (D) Continuous workflow: initial random sampling (27 recipes in this demo), automated droplet generation/transport, thermal reaction, *in situ* SAXS/WAXS, droplet identification via WAXS correlation, SAXS analysis for d and σ, *GP* modeling of $X \rightarrow Y$, and Bayesian optimization of the next batch (labels 1−7 map to panels A−C). (E) Droplet tracking: (I) continuous WAXS reveals distinct features for oil vs aqueous droplets in q-range 1−3 Å^{-1}; (II) real-time phase identification via correlation to an oil reference (score 1 for oil, 0 for aqueous).

Using citrate-reduced gold nanoparticles as a model system, two autonomous campaigns efficiently navigated ∼19,000 admissible recipes and reduced the number of actual required experiments by almost 2 orders of magnitude (to 365 measurements) for achieving precise control over defined experimental goals, such as particle size (4−60 nm) and polydispersity (σ < 0.11), while spanning citrate:gold ratios 0.27−480 (well beyond the traditional 1−10 window). Beyond validating classical Turkevich−Frens trends across this expanded space, we reveal previously inaccessible structure−synthesis relationships. Quantitative SAXS/WAXS analysis uncovers a parallel-band scaling between crystallite and particle sizes with a common slope, where synthesis chemistry tunes the intercept β to decouple crystallite coarsening from particle size. Complementary high-resolution transmission electron microscopy (HRTEM) images display multiple lattice-fringe orientations within single particles and corroborate the WAXS-derived finding that d_c is smaller than d and tunable at a fixed d. Complementary partial-dependence (PD) and ICE analyses quantify nonlinear, context-dependent effects of chemical recipes (gold, citrate, and pH) on the reaction products. Together, *in situ* structural feedback and GP-guided design provide a robust framework to map and control nanoparticle size and crystallinity across expansive chemical spaces, grounding autonomous optimization in a quantitatively validated, multiscale structure.

RESULTS AND DISCUSSION

Workflow of the Self-Driven Fluidics Platform for Real-Time Autonomous Synthesis. Our self-driven fluidic platform integrates a mobile synthesis workstation, *in situ* measurements, and machine-learning (ML) decision-making to enable high-throughput, closed-loop autonomous synthesis of colloidal nanoparticles (Figure 1). The loop proceeds in four steps. First, ML-guided experimental design (Figure 1.1), where ML models link synthesis parameters $\boldsymbol{X}$ (e.g., chemical reagents, concentrations, flow rate, mixing sequence, reaction temperature, and reaction time) to nanoparticle characteristics $\boldsymbol{Y}$ (e.g., size and polydispersity). These ML models incorporate practical constraints such as the droplet size, droplet spacing,

https://doi.org/10.1021/jacs.5c03875
J. Am. Chem. Soc. XXXX, XXX, XXX−XXX

and mechanical resolution. The models' predictions are directly translated into instructions for the synthesis hardware. The second step involves automated flow synthesis (Figure 1.2), where our mobile workstation performs precision liquid-flow control and temperature-regulated chemical reactions. The fluidic system dispenses and mixes chemical reagents according to ML-suggested recipes and combines them with a carrier oil phase to form isolated reaction droplets. These droplets are generated continuously, travel as a steady stream of microreactors, and enter an in-house reactor for high-temperature synthesis. At our typical flow rate (~80 μL/min) and ~100 °C, aqueous droplets remained stable, with no observable merging, splitting, or evaporation. Stability arises from (i) hydrophobic PTFE/Kapton flow paths that prevent wall wetting; (ii) silicone-oil spacers between droplets; and (iii) ~100 mbar back pressure to raise the aqueous boiling point. Third, *in situ* SAXS/WAXS characterizations of droplets at the synchrotron beamlines (Figure 1.3). Real-time analysis within the reactor, equipped with multiple X-ray transparent windows, provides direct structural information (Y) within the native reaction environment. This *in situ* characterization is crucial because nanoparticle features observed during growth can differ significantly from those obtained by conventional postsynthesis *ex situ* or *in line* methods (Y'). The fourth step is real-time data analysis, wherein SAXS/WAXS data are processed immediately to extract multiscale structural characteristics. Specifically, WAXS peak analysis reveals atomic arrangement (crystallinity), while SAXS form-factor modeling determines the nanoscale morphology (size, distribution, shape). The resulting X-Y pairs are fed back to the ML model, closing the loop. This iterative process optimizes synthesis parameters to achieve user-defined objectives with each subsequent experiment, strategically balancing exploration of new conditions and exploitation of promising regions in the parameter space.

Following our modular and mobile design concept (Figure 1), we constructed the synthesis workstation on a compact, transportable rack (Figure 2A, detailed in SI). Briefly, the workstation consists of three main modules: (1) a liquid-handler module (chemical reservoirs, multiple syringe pumps, liquid filters, gas-pressure controllers, valve controllers, and cross-mixer), (2) a chemical-reactor module (droplet reactor and temperature controller), and (3) *in situ* characterization tools (UV−vis spectroscopy in the chemistry lab). All modules are centrally controlled via a computer interface using custom Python scripts. Our in-house-designed droplet reactor incorporates two sandwiched aluminum plates with zigzag flow channels capable of accommodating glass or Kapton tubing. It is also equipped with heating cartridge heaters (up to 350 °C) and RTD sensors for PID temperature control. A 9 (columns) × 6 (rows) array of ports provides optical access, serving as windows for both UV−vis and X-ray *in situ* characterization during nanoparticle formation. Although the array of optical windows enables flexible time-resolved measurements across different stages, in this study, we fixed the reaction time and used a single X-ray window aligned to that position.

To validate our autonomous synthesis platform, we selected the well-studied Turkevich method[49−51] for gold nanoparticle synthesis as a proof-of-concept model system. We deployed our mobile platform at the CMS 11-BM and SMI 12-ID beamlines (Figure 2B−C) at Brookhaven National Laboratory's National Synchrotron Light Source II (NSLS-II). At these beamlines, the X-ray beam was aligned through the reactor's X-ray transparent window (Figure 2C), enabling real-time, *in situ* SAXS/WAXS analysis of nanoparticle morphology and crystallinity during synthesis.

The detailed workflow procedure and droplet flow are shown in Figure 2D (left and right panels, respectively), which illustrates how our platform achieves sequential, yet parallelized, autonomous operation. The functional steps of the platform are also highlighted in Figure 2A−C. A key feature of our system is its ability to conduct high-throughput synthesis under a steady, continuous flow while maintaining precise control individual reactions and monitoring for their outcomes. The process begins by initializing with randomly selected recipes (27 here) to match the number of droplets in the flow path before characterization. Droplets are continuously generated, each with an independent chemical composition (as three droplets are depicted in step 1 of Figure 2D). These droplets then sequentially flow into the reactor (droplet-1 in step 2 of Figure 2D) at a controlled temperature. Simultaneously, new droplets continue to be generated (up to 24 in step 2 of Figure 2D). As the flow continues, droplet-1 flows into the X-ray beam path and receives *in situ* SAXS/WAXS characterization (step 3 in Figure 2D). At a fixed flow rate, the axial position of the X-ray beam along the reactor sets the residence time at the characterization. Concurrently, due to the continuous flow, while droplet-1 is being probed by X-ray, subsequent droplets (e.g., droplets-2,3) are simultaneously progressing through the reactor. Consequently, chemical reactions proceed in parallel within all of the droplets residing inside the reactor. Typically, around 10 droplets reside within the reactor simultaneously, enabling parallel reaction processing. This parallel execution allows new droplets to be generated, while previous ones undergo characterization and analysis. To ensure that every droplet is captured, we continuously collect SAXS/WAXS frames.

This continuous and interleaved operation ensures tight workflow synchronization, reducing downtime, and enhancing experimental efficiency, but it also poses a critical challenge: accurately tracking and associating characterization data with corresponding chemical recipes and reaction conditions for each droplet. After generation, each droplet traverses the reactor for a fixed residence time before being characterized. While the number of droplets in the flow path can be controlled by adjusting flow rate, droplet volume, and spacing, practical issues, such as occasional bubble formation at high temperature, can alter this number. Even a single off-by-one pairing error between synthesis and characterization would misalign data and degrade the ML model's optimization. Because the GP model relies on accurate $\boldsymbol{X}$-$\boldsymbol{Y}$ mapping, such errors undermine data set integrity and downstream decision making.

To address this challenge, we developed a real-time droplet tracking method (step 4 of Figure 2D) based on correlation analysis of distinctive features in the WAXS data from the carrier oil and aqueous reaction phases. Specifically, as shown in Figure 2E−I, the oil phase exhibits a distinctive scattering feature in WAXS, characterized by a broad peak within the wave vector transfer (q) range from 1 to 3 Å^{-1}, which is absent in the aqueous phase. By correlating each frame's WAXS profile with a reference oil scattering profile (Figures 2E-II and S3), we can reliably differentiate oil segments (correlation score ~ 1) from aqueous droplets (correlation score ~ 0). Consistent droplet spacing/length over hundreds of events

https://doi.org/10.1021/jacs.5c03875
J. Am. Chem. Soc. XXXX, XXX, XXX−XXX

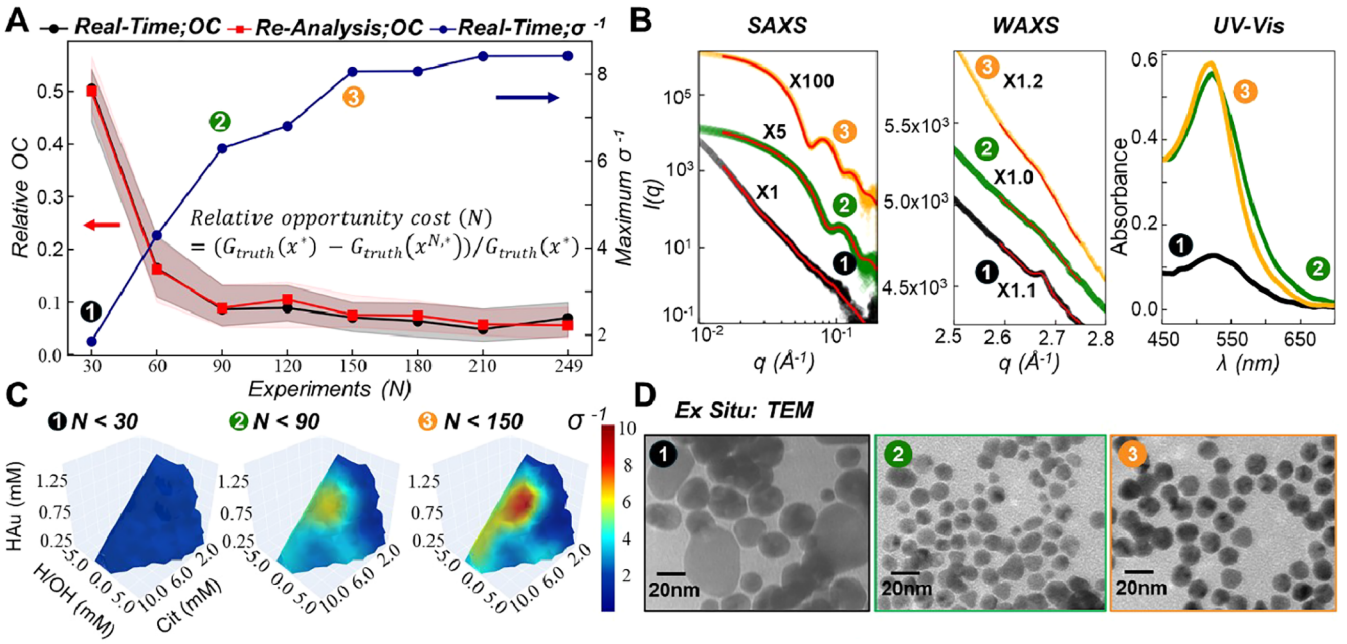

Figure 3. Autonomous synthesis of uniform Au nanoparticles guided by multimodal structure characterization. (A) Learning curve shows the best-predicted σ^{-1} (monodispersity proxy) increases as the data set grows (Run 1; N = 30 to 249), with relative opportunity cost (ROC) tracking convergence (black: real-time; red: postexperiment validation with standardized fitting ranges). (B) Representative *in situ* SAXS/WAXS with UV−Vis absorption spectra (both axes in SAXS are in logarithmic scales and both axes in WAXS are in linear scales) and (D) *ex situ* TEM at three stages (from A): (1) early random recipes (N < 30) show broad size distributions; (2) intermediate (N < 90) reaches $d \sim 9.8$ nm, $\sigma \sim 0.15$; (3) later (N < 150) reaches $d \sim 13.6$ nm, $\sigma \sim 0.11$. (C) Evolution of GP-predicted $1/\sigma$ maps in the 3-reagent volume space (μL) at N = 30, 90, 150, revealing rapid convergence to optimized synthesis conditions ($\sigma \sim 0.11$) within ∼150 experiments from a 19,000-combination design space.

further confirms the droplet integrity under the reaction conditions; anomalies that would indicate coalescence were not detected. Also, this clear contrast enables frame-accurate tracking of droplet boundaries through the reactor and unambiguous association of synthesis conditions with corresponding characterization data (see details in SI). We also benchmarked static versus flowing measurements using UV−Vis and SAXS/WAXS. Across 0−2000 μL/min, spectra and scattering profiles were indistinguishable (Figures S1−S2). During autonomous runs, we operated at ∼80 μL/min. To avoid oil−water interface contributions, the first/last frames of each droplet were excluded automatically and only the central segment was analyzed.

With droplet identity resolved, the workflow advances to data analysis (step 5 in Figure 2D). SAXS frames fit with a spherical form-factor model to extract the nanoparticle diameter and size distribution, while WAXS Bragg-peak analysis assesses crystallinity. These extracted structural parameters are then input into a Gaussian process machine-learning (GPML) model that maps reaction conditions $\boldsymbol{X}$ to nanoparticle features $\boldsymbol{Y}$ (step 6 in Figure 2D). Finally, Bayesian optimization (BO) within the GP framework selects the next synthesis conditions (step 7 in Figure 2D). The optimized recipe is sent back to step 1 to initiate new droplet generation (e.g., droplet-28 as the first ML-suggested recipe), thereby closing the loop and enabling iterative refinement of nanoparticle features to meet user-defined objectives.

Experimental Run 1: Autonomous Synthesis of Monodisperse Nanoparticles. To demonstrate the platform's capabilities, we conducted an initial autonomous campaign ("Run 1") that explored the synthesis space with a single objective: minimize the size polydispersity σ, (equivalently, maximize σ^{-1}). We employed a GP surrogate with the Upper Confidence Bound (UCB) acquisition function, $a_{\mathrm{UCB}}(x) = \mu(x) + \beta^{1/2}\sigma(x)$, with β = 100, to balance exploration and exploitation in a large, sparsely sampled space. For this proof of concept, we varied reagent volumes while holding the temperature (100 °C) and residence time (10 min) fixed. Recipes drew from three stock solutions: 10 mM sodium citrate (Cit), an acid/base titrant (10 mM HCl or NaOH, denoted "H/OH"), and 2 mM $HAuCl_4$ (HAu). Practical constraints were enforced: Cit and HAu each in 1−30 μL, titrant in 0−30 μL, and total droplet volume fixed at 40 μL by buffer backfill. At the typical flow rate (∼80 μL/min), each droplet yielded ∼10 frames of SAXS/WAXS (1 frame per second). Following the workflow in Figure 2D, the run began with 27 randomly chosen recipes (matching the precharacterization pipeline length), then proceeded with fully autonomous synthesis, encompassing synthesis, *in situ* characterization, real-time data analysis, GP update, and BO next recipe selection until termination after ∼10 h (249 droplet reactions). Human intervention was required to replenish only chemical reservoirs.

The progression of autonomous optimization is visualized in Figure S4A, which maps the observed σ^{-1} values in the 3D chemical volume space at eight representative experimental stages (N = 30, 60, 90, 120, 150, 180, 210, and 249). The system initially explored broadly; by $N \approx 61$−90, regions with $\sigma^{-1} > 6$ emerged and expanded thereafter. Using volumes as inputs $\boldsymbol{X}$ and σ^{-1} as outputs $\boldsymbol{Y}$, we trained successive GP models f_N. Three representative maps (N = 30, 90, 150) are shown in Figure 3C; final models trained on all Run-1 data (N = 249) for both σ^{-1} and d are in Figure S4B. Owing to the fixed 40 μL total, the feasible set occupies a constrained subvolume of the 3D space. Early models (N = 30) showed weak contrast and large uncertainty consistent with limited

https://doi.org/10.1021/jacs.5c03875
J. Am. Chem. Soc. XXXX, XXX, XXX−XXX

data; by N = 90 clear trends appeared, and by N = 150 the predicted landscapes sharpened substantially, reflecting improved structure−synthesis learning (see Figure S4B for details).

To quantitatively assess the GPML model's learning efficiency, we tracked the maximum predicted σ^{-1} value from each successive model f_N (Figures 3C and S4B). As shown in Figure 3A (navy profile), the maximum increased from ∼ 2 to 6 as the training data set grew from N = 30 to N = 90, with marginal gains beyond 150, reaching ∼9 at the end of Run 1. This trajectory indicates that ∼90 data points were sufficient to identify high-performing regions, with further refinement through ∼150 active-learning iterations. Notably, this efficient optimization, only using 150 experiments, effectively explored ∼19,000 feasible experimental conditions (as detailed in the Methods). We used a UCB acquisition with β = 100 to favor exploration early in such a large, sparsely sampled space, which helped avoid premature convergence while still enabling later-stage exploitation.

The effectiveness of this optimization is further corroborated by the SAXS profiles acquired at key stages (Figure 3B). For representative stages corresponding to N = 30, 90, and 150, we selected three chemical recipes (R1, R2, and R3) closely matching those predicted by the f_N models. The initial recipe R1 produced nanoparticles with a featureless SAXS profile, which, upon curve-fitting, indicated high polydispersity ($\sigma \sim$ 1). After 90 experiments, the optimized recipe produced less polydisperse nanoparticles with clear spherical form-factor features in their SAXS profile, yielding a diameter (d) of ∼9.8 nm and $\sigma \sim$ 0.15. Between the 121st and 150th experiments, nanoparticle uniformity was further improved, generating particles with an average d of ∼13.6 nm and $\sigma \sim$ 0.11, which is comparable to or exceeding commercial standards.

Beyond SAXS-derived nanoparticle size information, the particle internal atomic structure, such as degree of crystallinity, was probed by WAXS by monitoring a (111) diffraction peak at $q \sim 2.68$ Å^{-1} of Au, a characteristic of gold face-centered cubic (FCC) lattice with a lattice parameter of ∼4.08 Å. In Figure 3B, the initial recipe (R1) exhibits a relatively sharp (111) peak, consistent with a larger crystalline size, larger coherent domain size, whereas later recipes (R2 at N = 61−90 and R3 at N = 121−150) show broader peaks, indicating smaller domains based on the Scherrer size-full width at half-maximum (FWHM) relationship. The quantitative relationship between the particle diameter and crystallite domain size is analyzed in detail later (Figure 6).

To highlight the advantages of direct *in situ* structural characterization by SAXS/WAXS, we conducted a parallel synthesis of recipes R1−R3, employing *in situ* UV−vis spectroscopy in a conventional chemistry laboratory setting. In contrast to the dramatic changes observed in SAXS profiles, the corresponding UV−vis spectra show less distinct changes, with surface plasmon resonance (SPR) peaks centered at 520−525 nm and peak widths decreasing from ∼140 to 100 nm (Figure 3B). UV−vis spectroscopy presents inherent complexities in data interpretation for gold nanoparticles. The SPR peak position depends not only on particle size but also on morphology, aggregation, and the dielectric environment,[52−54] while peak width incorporates contributions from homogeneous broadening and shape variations beyond polydispersity.[55,56] These convoluted signals make UV−vis less effective for providing quantitative feedback for autonomous optimization, whereas SAXS directly returns the size and distribution via form-factor fits.

We also examined these three nanoproducts using *ex situ* TEM observation. The postreactor samples were collected immediately, centrifuged three times at ∼21,000g (10−20 min) with supernatant exchange to quench reactions and remove precursors, drop-cast on Cu grids, and dried overnight prior to imaging. The TEM images (Figure 3D) corroborated the SAXS results, showing a clear progression toward tighter size distributions from R1 to R3, with initial large, polydisperse particles (4−50 nm in diameter, $\sigma \approx 1$) evolving into uniform particles ($d \approx$ 13.0 nm, $\sigma \approx$ 0.1).

To quantify optimization performance, we compute relative opportunity cost (ROC), defined as the relative difference in expectation between the true best input and the predicted best input at a given experimental number N, using the following equation

$$\mathrm{ROC}(N) = \left| \frac{(G_{\mathrm{truth}}(x^*) - G_{\mathrm{truth}}(x^{N,*}))}{G_{\mathrm{truth}}(x^*)} \right|$$

where x^* represents the true best input (recipes), and $G_{\mathrm{truth}}(x^*)$ the maximum objective function (σ^{-1}) across the feasible space. We trained a final GPML model on all 249 experiments to serve as the G_{truth}, yielding optimal parameters x^* of 4.8 mM Cit, 1.75 mM NaOH, and 0.95 mM HAu. For a given N, the model G_N identifies the best input $x^{N,*}$ and its associated value σ^{-1}. The black profile in Figure 3A shows that as the GPML model is interactively trained with more data, $G(x^{N,*})$ converges toward the true maximum, $G_{\mathrm{truth}}(x^*)$, thereby minimizing the ROC. The ROC curve exhibits rapid improvement initially and plateaus after about 90 experiments, indicating that near-optimal performance is achieved with relatively few iterations compared to the large synthesis space. Moreover, our real-time automated SAXS curve-fitting is robust, as evidenced by similar *ROC* curves from both automated and postbeamtime analysis (Figures 3A and S6). We also observed an exponential decay in the difference between the predicted σ^{-1} values for the final optimal recipe (from G_{truth}) and those predicted at each stage (G_N), further validating the rapid initial learning and subsequent refinement characteristic of the UCB100 exploration-exploitation strategy (Figure S7).

We benchmarked active learning against a conventional grid-scan experiment (265 points) over parameter ranges typical of the literature with narrow pH variations.[50,51,57] Training a GP on the grid-scan data identifies an optimum within that restricted region (6 mM Cit, 0.75 mM NaOH, and 0.7 mM HAu) with $\sigma \sim$ 0.12 (e Figure S8). In contrast, our UCB-guided campaign achieved $\sigma \sim$ 0.11 with fewer experiments (249 vs 265) while exploring a far larger design space and discovering high-performance regimes beyond the conventional bounds (Figure S4). This comparison highlights the efficiency advantage of uncertainty-aware exploration in broad chemical spaces: similar or better outcomes with fewer total experiments and substantially greater coverage.

Experimental Run 2: Size-Targeted Autonomous Synthesis of Monodisperse Nanoparticles. Building upon the global optimization of size distribution achieved in Run 1, we extended our approach in Run 2 to minimize the size distribution for a specific target size. To this end, we defined an objective function that simultaneously incorporates both particle size and monodispersity

https://doi.org/10.1021/jacs.5c03875
J. Am. Chem. Soc. XXXX, XXX, XXX−XXX

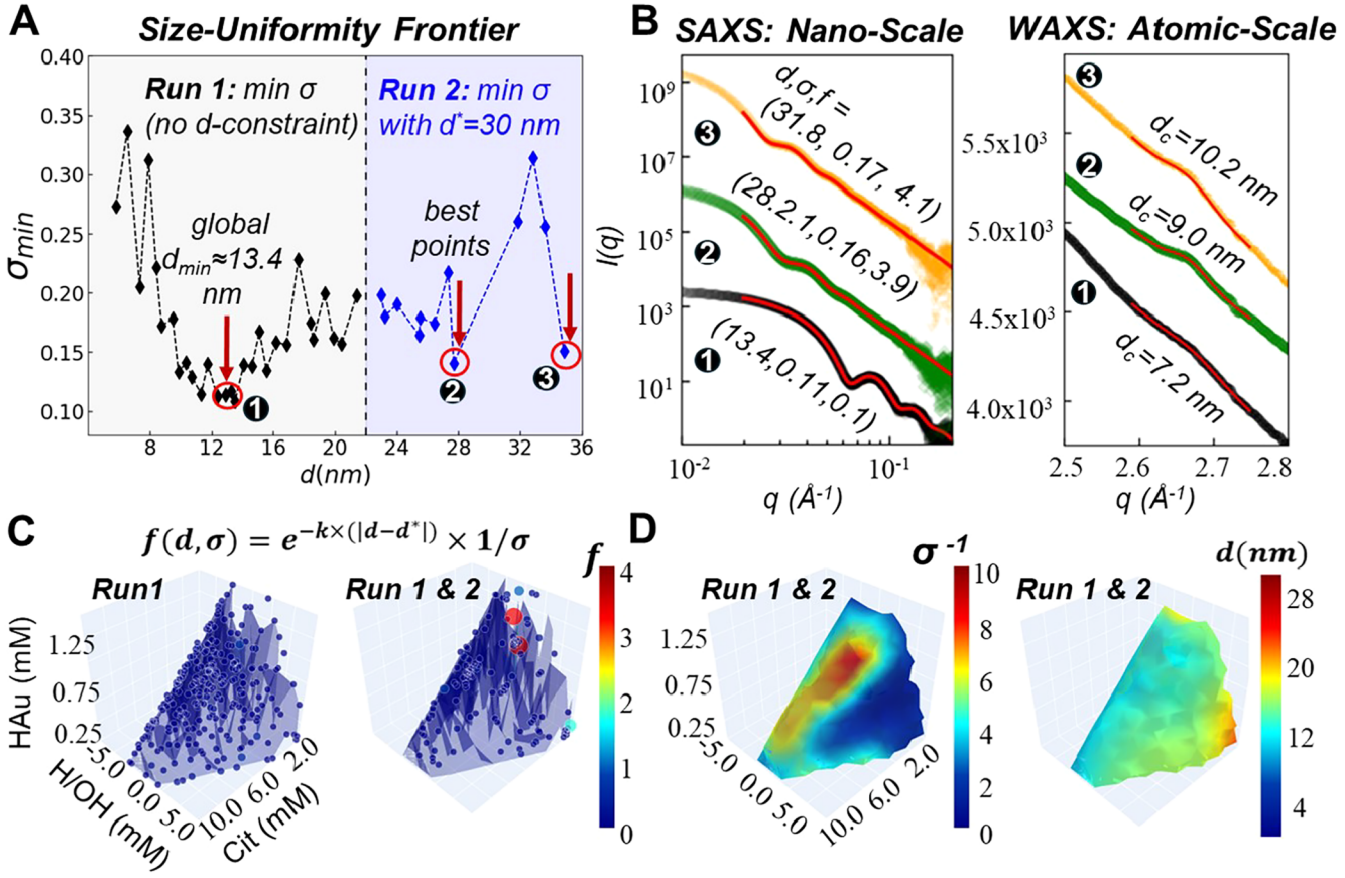

Figure 4. Autonomous synthesis of target size, uniform Au nanoparticles. (A) Size-uniformity frontier: minimum observed σ vs binned d derived from 249 (d,σ) pairs (Run 1; silver), and Run 2 (blue), which optimizes σ under a size constraint (objective f; see Methods). Labels denote: (1) global minimum σ; (2−3) two top-scoring recipes after Run 2 with target d^* = 30 nm. (B) SAXS and WAXS for the labeled recipes (both axes in SAXS are in logarithmic scales, and both axes in WAXS are in linear scales). (C) Objective-function landscape: low values in Run 1 and emergence of high-value regions after Run 2. (D) GP maps trained on combined Runs 1−2 (N = 365) for σ^{-1}(left panel) and d (right panel).

$$f(d,\sigma) = e^{-k|d-d^*|}/\sigma$$

where k is a scale factor (set to 0.5), d is the measured nanoparticle diameter from SAXS analysis, d^* is the target diameter (set to 30 nm), and σ is the relative size distribution from the SAXS fit. As shown in Figure S9, this function reaches its maximum when particles achieve both the target size and minimal size distribution. We intentionally selected a target diameter of 30 nm, well beyond the maximum d (22 nm) achieved in Run 1 (Figure S10), to demonstrate our platform's ability to access previously unexplored synthetic conditions.

To contextualize Run 2, we first quantified the Run 1 diameter − sigma landscape by binning the 249 (d,σ) pairs and extracting the minimum σ within each diameter bin. The resulting "uniformity frontier" (black squares, Figure 4A) shows a global σ minimum with d near 12−14 nm. A representative SAXS profile from this region (Figure 4B, trace 1) yields $d \approx 13.4$ nm with $\sigma \approx 0.11$. The blue shading in Figure 4A marks $d > 22$ nm that were not sampled in Run 1. Consistently, evaluating $f(d,\sigma)$ on the Run 1 GP map (Figure 4C, left) produces subunit maxima (<1), indicating that the synthesized particles were far away from the targeted 30 nm region.

Guided by this new object function, the same GP/UCB (β = 100) directed 116 additional autonomous experiments while maintaining experimental parameter constraints. Interestingly, as the campaign progressed, the system sampled larger particles ($d > 22$ nm) and achieved objective values $f > 1$ (Figure S10). The updated diameter—uniformity frontier (blue squares, Figure 4A) extends to $d \sim 36$ nm. The GP map of $f(r,\sigma)$ (Figure 4C, right panel) shows two top optima ($f \sim 4.1$ and 3.9), at (Cit, H/OH, HAu) = (0.4, 0, 0.8) mM and (0.8, 0.25, 0.85) mM, delivering (d,σ) = (31.8 nm, 0.17) and (28.2 nm, 0.16), respectively, close to the d^* = 30 nm target with competitive size uniformity.

Figure 4B compares SAXS and WAXS for three representative conditions: (1) the global minimum of σ from Run 1, (2−3) the top two Run 2 optima near d^*. These traces report nanoscale morphology (SAXS) together with atomic-scale order (WAXS). The WAXS (111) widths indicate crystalline domains smaller than particle diameters, consistent with polycrystallinity; quantitative crystallite analysis and domain−particle decoupling are developed in Section 5 (Figure 6).

Finally, we retrained GP models on the combined data set (Run 1: 249 + Run 2: 116 = 365 experiments) to update the maps for both sigma and diameter in Figure 4D. Compared with the Run 1 map (Figure S4B), the sigma map remains largely unchanged, confirming Run 1's efficiency in exploring synthesis space for monodispersity. In contrast, the diameter map now clearly shows a new region of larger particles around 30 nm, directly reflecting our updated objective function. Together, these results highlight the adaptability and sample-efficiency of the platform: once an objective is specified, the

https://doi.org/10.1021/jacs.5c03875
J. Am. Chem. Soc. XXXX, XXX, XXX−XXX

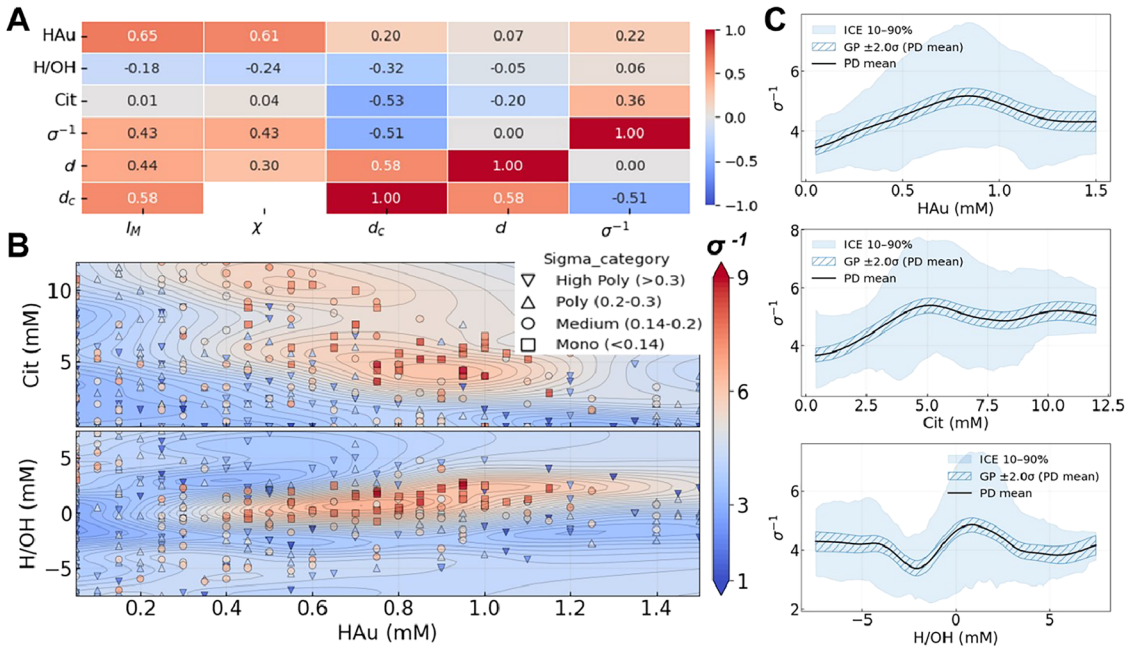

Figure 5. Quantitative relationships between synthesis variables and nanoparticle characteristics. (A) Spearman correlation heat map relating synthesis variables (HAu, Cit, and signed-titrant pH proxies for HCl/NaOH) to SAXS/WAXS outputs: σ^{-1}, d (SAXS), I_M at q = 0.01 A^{-1}, crystalline domain size d_c (WAXS), and crystallinity (χ; 0/1). (B) 2D partial-dependence (PD) surfaces for σ^{-1} vs (HAu, Cit) (top) and vs (HAu, pH) (bottom). PD values are GP posterior means averaged over the empirical distribution of the remaining inputs; experimental recipes are overlaid with categorical markers and a shared colorbar. (C) 1D PD and individual conditional expectation (ICE) for σ^{-1} vs HAu, Cit, and pH. Solid line: PD mean; hatched band: PD mean ± 2 GP-prediction uncertainty; light band: ICE central 80% (10–90th percentile across baselines). (B, C) Partial-dependence analysis revealing nonlinear coupling between synthesis variables, with narrow ICE bands indicating robust main effects versus wide bands showing context-dependent interactions.

loop navigates toward target properties with minimal additional experiments and without human intervention.

Revealing Relationship between Reaction Conditions and Nanoparticle Characteristics. Our autonomous platform generated a comprehensive multiscale data set spanning citrate: gold molar ratios from 0.27 to 480, well beyond the traditional 1–10 window explored in classical Turkevich–Frens syntheses.[49−51,58,59] With 365 experiments combining SAXS and WAXS measurements, this data set enables systematic analysis of synthesis-structure relationships across a large parameter space. Here, we examine how reaction conditions influence nanoparticle characteristics through three complementary approaches: global correlation analysis to identify primary trends, partial-dependence modeling to reveal nonlinear interactions, and combined SAXS/WAXS analysis to probe the relationship between the particle size and internal crystalline structure.

Global Correlation Analysis. We first computed Spearman rank correlations between synthesis variables (HAu, pH modifier volume, Cit) and nanoparticle characteristics: uniformity (σ^{-1}), diameter (d), crystallite domain size from WAXS (d_c), crystallinity (χ = 0/1), and maximum SAXS intensity (I_M at q = 0.01 $Å^{-1}$). As shown in Figure 5A (full matrix in Figure S11), uniformity shows a moderate positive correlation with Cit (ρ = 0.36), consistent with Cit's established role in promoting numerous, well-capped nuclei that yield tighter distributions.[28,51] Notably, uniformity is essentially uncorrelated with diameter ($\rho \approx 0.00$), indicating that monodispersity and size can be tuned somewhat independently, presenting a useful decoupling for targeted synthesis. Diameter shows a weak negative correlation with Cit (ρ = −0.20), aligning with the canonical inverse size–citrate relationship,[49−51] while its global correlations with pH (−0.05) and HAu (+0.07) are small because the effects are strongly context-dependent rather than globally linear. As expected from physical considerations, diameter correlates with crystallite size (ρ = 0.58) and with SAXS intensity (ρ = 0.44), since larger particles scatter X-rays more strongly. Crystallite size anticorrelates with Cit (ρ = −0.53) and, more moderately, with base addition (ρ = −0.32), suggesting that Cit and effective charge suppress domain coarsening, which is consistent with stronger surface stabilization.[59] I_M correlates strongly with HAu (ρ = 0.65) and with crystallinity (ρ = 0.85), reflecting that more reduced Au yields more scatterers and more frequent Au(111) peaks; however, it shows negligible correlation with Cit and only modest correlation with uniformity, underscoring that intensity is not a proxy for monodispersity. I_M primarily reflects the amount, size, and crystallinity rather than the distribution width. Overall, while these global correlations confirm several canonical trends, Spearman coefficients cannot reveal interactions or non-monotonic effects. Several variable pairs show modest correlations even when strong context-dependent relationships exist, motivating our next nonlinear, interaction-aware analysis.

Nonlinear Interactions via Partial Dependence. To quantify marginal and interaction effects, we computed partial dependence (PD) and individual conditional expectation (ICE) from the trained Gaussian-process models. For each variable, PD reports the model-predicted response averaged over the empirical distribution of the other inputs; ICE curves show the response for fixed baseline recipes as the variable is swept. We visualized the GP's predictive uncertainty along the PD sweep (±2σ hatched band) and the central 80% ICE envelope (10th to 90th percentile, light band), which captures

https://doi.org/10.1021/jacs.5c03875
J. Am. Chem. Soc. XXXX, XXX, XXX−XXX

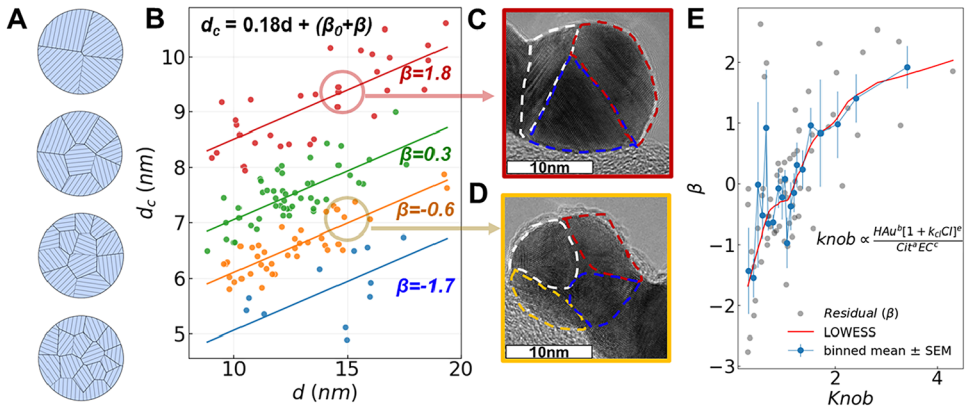

Figure 6. Decoupling crystallite coarsening from particle growth reveals independent structural control. (A) Schematic illustration of a particle with the same diameter but increasing crystallite domain size (bottom to top). (B) Discovery of parallel crystallite scaling bands ($d_c = 0.18d + (\beta_0 + \beta)$) indicating recipe-tunable coarsening at fixed particle size. Within crystalline SAXS particles (d, 8−20 nm, 114 data points), $\beta_0 \sim 5$ is the average of the intercept, and β changes from ∼3 to ∼3 nm. K-means clustering on residuals (β) identifies intercept-separated bands (colors), consistent with recipe-dependent coarsening at fixed d. (C, D) HRTEM from two recipes (red/orange bands) with similar $d \approx 15$ nm but different d_c (∼9 and ∼6.5 nm). (E) Residual vs chemistry knob: residual increases monotonically with a constrained power-law "knob" (definition shown in E), showing strong association (cross-validated Spearman $\rho \sim 0.7 \pm 0.1$). Gray points are recipes; the blue line/band is binned summary statistics (median with 10−90%); the red curve is LOWESS (locally weighted, nonparametric regression). Positive elasticities for HAu/Cl and negative for Cit/EC (effective charge) indicate chloride/precursor-biased coarsening moderated by citrate/base.

recipe-to-recipe heterogeneity. The 2D PD surfaces for σ^{-1} (Figure 5B) recover the familiar "good-uniformity" corridor at intermediate Cit (4−6 mM) and moderate base with sufficient HAu (0.6−1.0 mM) and neutral-to-mildly basic pH, which agrees with the regime associated with reliable Turkevich synthesis.[50] However, the surfaces make coupling explicit: benefits of increasing HAu depend critically on being within the right Cit/pH corridor; outside this region, it gains taper or reverse. This explains why global HAu-uniformity correlation appears modest (ρ = 0.22) despite strong local effects.

The 1D PD/ICE analysis (Figure 5C) provides complementary insights. For HAu, a pronounced PD peak appears around 0.8 mM, but the wide ICE envelope indicates that precursor effects are highly recipe dependent. For Cit, PD peaks at intermediate values (5 mM) with a broad ICE envelope, confirming that while Cit generally improves uniformity, the magnitude depends on pH and HAu. For pH, acidic conditions (≈−3 mM HCl addition) consistently degrade uniformity σ^{-1} (narrow ICE band), matching literature reports that acid weakens citrate's capping ability.[28,49,58] Near-neutral-to-mildly basic conditions show PD improvement with wide ICE bands, indicating that the base can substantially improve uniformity for some but not all recipes.

For diameter (Figure S12), Cit shows saturating behavior: above ∼8 mM, both PD and ICE converge to consistently small particles, while at low Cit (∼2 mM) the wide ICE band reveals strong dependence on pH/HAu context. pH effects are clear: acidic conditions yield larger particles with variable outcomes (wide ICE), while basic conditions consistently produce smaller particles (narrow ICE), aligning with reports that hydroxide substitution slows precursor reactivity and favors controlled growth.[51,57]

Discovery of Decoupled Crystallite-Particle Scaling. Having established how synthesis parameters affect individual characteristics, we examined the relationship between the crystallite and particle sizes using joint SAXS/WAXS analysis. For crystalline samples within a common size window ($d \approx 8$−20 nm; 114 points after filtering), regressing WAXS-derived crystallite size (d_c) against SAXS particle diameter (d) revealed a single common-slope fit captures the global trend, $d_c \approx m \cdot d + \beta_0$, with $m \approx 0.18$ and $\beta_0 \approx 5$ nm. We then defined a per-recipe residual $\beta = d_c - (m \cdot d + \beta_0)$, i.e., the residual intercept a particle would have at that slope (Figure 6B). These residual isolates crystallite coarsening at fixed particle size: positive β means larger domains than expected for a particle of that d, and negative β means smaller. K-means clustering of these residuals identified four intercept-separated bands spanning roughly −1.7 to +1.8 nm about an average intercept near 5 nm. This parallel structure means that at any fixed particle diameter, crystallite domain size can vary by several nanometers depending on synthesis chemistry, which presents a tunable internal degree of freedom not predicted by simple Cit, HAu, or pH heuristics.

Direct imaging validates that these intercept shifts are structural. HRTEM on samples obtained from the two recipes with matched diameters ($d \approx 15$ nm) but drawn from different bands shows polycrystalline interiors with distinct domain sizes (∼9 versus ∼6.5 nm), consistent with their WAXS-derived d_c values and band assignments (Figure 6C−D). Thus, the "parallel-band" structure reflects genuine differences in crystallite coarsening at fixed d, not artifacts of peak fitting.

To identify chemistry drivers of the intercept β, we constructed a constrained power-law "chemistry knob" that increases with the precursor and chloride and decreases with the Cit and effective charge (EC): knob ∝ $HAu^b(1 + K_{Cl}Cl^e)/(Cit^aEC^c)$. Fitting non-negative exponents to the GP-inferred residuals yielded ≈ 0.55, $b \approx 0.39$, $e \approx 0.23$, $c \approx 0.21$ ($k_{cl} = 1$), with a strong monotone association with β under cross-validation (Spearman $\rho \approx 0.7 \pm 0.1$; Figure 6E). These sublinear exponents indicate diminishing returns in chemistry control. Doubling HAu increases the knob by ∼31% ($2^{0.39}-1$), while doubling Cit decreases it by ∼32% ($1-2^{-0.55}$). Doubling the effective charge (EC) produces a smaller ∼14% decrease ($1-2^{-0.21}$), and the chloride effect varies with baseline concentration, reaching at most ∼17% increase when doubled. Since crystallite size at fixed particle diameter increases

https://doi.org/10.1021/jacs.5c03875
J. Am. Chem. Soc. XXXX, XXX, XXX−XXX

monotonically with the knob value, these percentage changes translate directly to shifts in crystallite domains.

This sublinear response ensures robust control in such a way that even large changes in synthesis chemistry produce moderate, predictable adjustments in crystallite size rather than extreme variations, making the system practical for targeted synthesis. This provides a quantitative control mechanism: higher precursor and chloride concentrations drive recipes toward larger crystallite domains at fixed particle size (positive elasticities), while Cit and base suppress coarsening (negative elasticities). From the chemical insight perspective, chloride-rich, precursor-rich conditions may favor domain growth through moderated reduction kinetics that enable defect healing or oriented attachment, while Cit and base stabilize surfaces and inhibit coarsening, which is consistent with their known roles in nanoparticle synthesis.[58,59]

Together, these analyses demonstrate that the particle size and crystallite domain size are partially decoupled control parameters. The common slope reflects baseline coupling between growth and coarsening, while chemistry selects the intercept band, which provides an independent handle on internal crystalline order invisible to UV−vis but revealed through autonomous exploration with joint SAXS/WAXS characterization.

CONCLUSIONS

We developed an autonomous synthesis platform integrating a droplet-flow microreactor with *in situ* SAXS/WAXS measurements and Gaussian process optimization to map and control nanoparticle structure during reaction. Through two closed-loop campaigns totaling 365 experiments, the system efficiently explored ∼19,000 possible synthesis conditions, achieving precise control over gold nanoparticle size (4−60 nm) and polydispersity (σ < 0.11) while extending far beyond traditional synthesis boundaries (citrate:gold ratios 0.27−480 versus conventional 1−10). Extensive validation confirmed measurement reliability: static versus flowing conditions yielded identical results, droplets remained stable at 100 °C, and run-to-run variations stayed below 5%.

The platform's real-time structural feedback enabled the discovery of previously inaccessible synthesis-structure relationships. Partial-dependence and ICE analyses revealed strongly context-dependent effects, explaining why simple correlations fail to capture the full parameter space behavior and identifying robust versus interaction-dominated synthesis regimes. Most significantly, joint SAXS/WAXS analysis uncovered decoupled control over the particle size and crystallite domains. The parallel-band scaling relationship, $d_c \approx 0.18 \cdot d + \beta$, demonstrates that crystallite size can be tuned independently at fixed particle diameter through a quantitative chemistry knob, where precursor and chloride promote coarsening while citrate and base suppress it (cross-validated Spearman $\rho = 0.7 \pm 0.1$).

This finding provides a practical design principle: internal crystalline order represents an additional control parameter beyond particle size and dispersity that can be accessed through specific chemical adjustments but is invisible to conventional optical characterization. The modular platform design enables extension to other chemistries and synchrotron techniques (XAS, XPCS, and PDF), as well as time-resolved studies using multiple reactor windows. By combining high-throughput autonomous experimentation with multiscale *in situ* characterization, this approach establishes a general framework for discovering and exploiting hidden degrees of freedom in nanomaterial synthesis.

EXPERIMENTAL PROCEDURES

Materials. Sodium citrate (Cit), hydrogen chloride (HCl), sodium hydroxide (NaOH), tween20, chloroauric acid (HAu), and silicone oil were purchased from Sigma-Aldrich. Stock solutions, including 16 mM Cit, 2 mM HAu, 10 mM HCl, 10 mM NaOH, 0.01 wt % tween20 in deionized (DI) water, and silicone oil, were prepared and transferred to 10 mL of gastight glass syringes (Hamilton Inc.) for automated nanoparticle synthesis.

Fluidic Platform. The fluidic platform enables high-throughput nanoparticle synthesis with *in situ* small- and wide-angle X-ray scattering (SAXS/WAXS) characterization. As shown in Figure 2, the system comprises: (i) syringe pumps (New Era Systems and KEM pumps) with gastight glass syringes, (ii) a solution filtration system preventing bubble formation, (iii) selection valves (M-Switch; Fluigent Inc.) and a static mixer (PTFE helixes) for reagent selection without cross-contamination and mixing, (iv) a customized flow reactor (∼120 mm × 90 mm) with temperature control up to 350 °C, (v) a temperature controller (Lakeshore), and (iv) a back-pressure system (Fluigent EZ-gas Pump) preventing bubble expansion at high temperature. Poly(tetrafluoroethylene) (PTFE) tubing (1/8″ OD, 1/16″ ID) forms the main flow path, with Kapton tube (0.110″ OD, 0.105″ ID) in the flow reactor for X-ray measurements. The Kapton tubing received hydrophobic treatment by Rain-X to ensure stable aqueous-in-oil droplet formation and smooth droplet movement. The system was installed at both SMI (12-ID) and CMS (11-BM) beamlines at the National Synchrotron Light Source II (NSLS-II), Brookhaven National Laboratory. All the hardware, including syringe pumps, cross-mixers, and a temperature controller, was fully controlled by custom Python scripts. In addition to synchrotron-based SAXS/WAXS measurements, the autonomous synthesis platform also integrates *in situ* UV−vis characterization in a general laboratory setting, enabling real-time optical UV−vis monitoring during the synthesis. The detailed setup for UV−vis integration in the chemistry laboratory is shown in the Supporting Information (Figure S1). To confirm the robustness of the system, we validated droplet stability and flow-rate effects on spectral quality prior to autonomous synthesis; details are provided in the Supporting Information (Figure S2).

Automated Nanoparticle Synthesis and Characterization. Reagent solutions (Cit, tween in DI water, HCl, NaOH, and HAu) were precisely injected using automated syringes with precisely controlled volumes (precision <1 uL) and flow rate at 80 uL/min through selection valves into the main flow loop, then undergoing well-mixing with a static mixer. Subsequent oil injections created segmented flow (oil-in-aqueous phases) for high-throughput, parallel synthesis. Synthesis parameters were constrained to a minimum 1 mL Cit/HAu, variable HCl/NaOH, 1 uL step size, 40 uL total volume (balanced with 0.01% tween20), and 60 uL oil spacing. The concentration limits are [0.4, 12], [−7.5, 7.5], and [0.05, 1.5] mM for Cit, HCl/NaOH, and HAu, respectively. Since we either add acid or base, we accordingly donate negative and positive signs for the concentration of HCl and NaOH. Reaction conditions were maintained at 100 °C, with as-synthesized products being probed at 10 min. *In situ* SAXS/WAXS (beamline details in SI) provided real-time size/distribution information, feeding ML models that suggested subsequent conditions to enable an on-the-fly closed-loop process. Using identical recipes and reaction conditions, we performed *in situ* UV−vis spectroscopy and *ex situ* TEM analysis. For TEM, aqueous droplets were collected immediately after exiting the reactor and subjected to centrifugation at ∼21,000*g* for 10−20 min (repeated three times) to rapidly quench the reaction and remove excess reagents. The purified samples were then deposited on copper TEM grids and dried overnight under ambient conditions before imaging (JEOL 1400). The high-resolution transmission electron microscopy (HRTEM) observations were performed on a FEI Talos F200X operated at 200 kV.

https://doi.org/10.1021/jacs.5c03875
J. Am. Chem. Soc. XXXX, XXX, XXX−XXX

Machine Learning (ML). A Gaussian process (GP) model was used to map synthesis-structure relationships with Bayesian optimization (BO) guiding subsequent experiments. We utilized the Upper Confidence Bound (UCB) acquisition function: $a_{UCB}(x) = \mu(x) + \beta^{1/2}\sigma(x)$, where $\mu(x)$ and $\sigma(x)$ represent the GP mean and standard deviation at point x, respectively. In our implementation, we set $\beta = 100$ to promote an aggressive exploration in the early phase of optimization. This choice is motivated by the large parameter space (~19,000 conditions) and relatively small experimental budget (249 runs), where a high β helps avoid premature convergence and ensures effective sampling of diverse regions. This strategy is commonly adopted in BO frameworks under sparse, high-dimensional conditions, and it aligns with the theoretical recommendations in the GP-UCB framework. The model implementation used open-source Python libraries GPyTorch and BoTorch, incorporating customized penalty functions and workflow designs specific to our autonomous synthesis. Three reagent volumes of Cit, pH (HCl as negative or NaOH as positive values), and HAu were used as the input parameters, and the characterization outcome ($1/\sigma$) or objective-function value was used as the output parameter. During autonomous operations, the system optimized the acquisition function at each experimental step using the current GP fit, with the function's maximum determining subsequent experimental conditions.

■ ASSOCIATED CONTENT

Data Availability Statement

Data and code availability. All data supporting the findings of this study are available within the paper and Supporting Information files.

Supporting Information

The Supporting Information is available free of charge at https://pubs.acs.org/doi/10.1021/jacs.5c03875.

Additional experimental details, including synchrotron beamline setup and data analysis procedures, experimental results and analysis, grid-scan experiment comparisons; GP model, partial-dependence analysis, WAXS Scherrer analysis, parallel-band analysis, chemistry knob model, summary table of reported literature on AI-based platforms for material synthesis (PDF)

■ AUTHOR INFORMATION

Corresponding Author

Yugang Zhang − *Center for Functional Nanomaterials, Brookhaven National Laboratory, Upton, New York 11973, United States;* orcid.org/0000-0002-7832-1475; Email: yuzhang@bnl.gov

Authors

Hyeong Jin Kim − *Center for Functional Nanomaterials, Brookhaven National Laboratory, Upton, New York 11973, United States;* orcid.org/0000-0001-9180-0430

Matthew R. Carbone − *Computing and Data Sciences Directorate, Brookhaven National Laboratory, Upton, New York 11973, United States*

Fang Lu − *Center for Functional Nanomaterials, Brookhaven National Laboratory, Upton, New York 11973, United States;* orcid.org/0000-0003-3765-7615

Xiaohui Qu − *Center for Functional Nanomaterials, Brookhaven National Laboratory, Upton, New York 11973, United States*

Kristofer Reyes − *Computing and Data Sciences Directorate, Brookhaven National Laboratory, Upton, New York 11973, United States; Department of Materials Design and Innovation, University at Buffalo, Buffalo, New York 14260, United States*

Honghu Zhang − *Center for Functional Nanomaterials, Brookhaven National Laboratory, Upton, New York 11973, United States;* orcid.org/0000-0003-1784-7825

Lihua Zhang − *Center for Functional Nanomaterials, Brookhaven National Laboratory, Upton, New York 11973, United States;* orcid.org/0000-0003-3331-2345

Oleg Gang − *Center for Functional Nanomaterials, Brookhaven National Laboratory, Upton, New York 11973, United States; Department of Chemical Engineering and Department of Applied Physics and Applied Mathematics, Columbia University, New York City, New York 10027, United States; Center for Nanomedicine, Institute for Basic Science (IBS) and Department of Nano Biomedical Engineering (NanoBME), Advanced Science Institute, Yonsei University, Seoul 03722, Republic of Korea;* orcid.org/0000-0001-5534-3121

Complete contact information is available at: https://pubs.acs.org/10.1021/jacs.5c03875

Author Contributions

[▽]Y.Z.: Lead contact. Further information and requests for resources should be directed to and will be fulfilled by the lead contact, Y.Z. (yuzhang@bnl.gov).

Notes

The authors declare the following competing financial interest(s): We declare that a non-provisional patent application entitled "Next-Generation Fluidics Technology for Efficient Autonomous Synthesis of Colloidal Nanoparticles," which is related to the technology described in this manuscript, has been filed with the U.S. Patent and Trademark Office (USPTO) on January13, 2025, under Application No. 19/018,789.

■ ACKNOWLEDGMENTS

This research is supported by the Brookhaven National Laboratory (BNL), the Laboratory Directed Research and Development (LDRD) Grants: No. 22-059, "Precision synthesis of multiscale nanomaterials through AI-guided robotics for advanced catalysts", No. 24-004, "Human-AI-facility integration for the multimodal studies on high-entropy nanoparticles.", and the Division of Chemical Sciences, Geosciences, & Biosciences, Office of Basic Energy Sciences, Department of Energy, under contract DE-SC0012704 at Brookhaven National Laboratory (FWP CO-060). This research also used resources of the Center for Functional Nanomaterials, the CMS (11-BM) and SMI (12-ID) Beamlines, and resources of the National Synchrotron Light Source II, which are U.S. Department of Energy Office of Science User Facilities, at Brookhaven National Laboratory under Contract No. DE-SC0012704.

■ REFERENCES

(1) Baek, W.; Chang, H.; Bootharaju, M. S.; Kim, J. H.; Park, S.; Hyeon, T. Recent advances and prospects in colloidal nanomaterials. *JACS Au* **2021**, *1* (11), 1849−1859.

(2) Wang, L.; Kafshgari, M. H.; Meunier, M. Optical properties and applications of plasmonic-metal nanoparticles. *Adv. Funct. Mater.* **2020**, *30* (51), No. 2005400.

(3) Shi, Y.; Lyu, Z.; Zhao, M.; Chen, R.; Nguyen, Q. N.; Xia, Y. Noble-metal nanocrystals with controlled shapes for catalytic and electrocatalytic applications. *Chem. Rev.* **2021**, *121* (2), 649−735.

(4) Howes, P. D.; Chandrawati, R.; Stevens, M. M. Colloidal nanoparticles as advanced biological sensors. *Science* **2014**, *346* (6205), No. 1247390.
(5) Talapin, D. V.; Lee, J.-S.; Kovalenko, M. V.; Shevchenko, E. V. Prospects of colloidal nanocrystals for electronic and optoelectronic applications. *Chem. Rev.* **2010**, *110* (1), 389−458.
(6) Thanh, N. T. K.; Maclean, N.; Mahiddine, S. Mechanisms of nucleation and growth of nanoparticles in solution. *Chem. Rev.* **2014**, *114* (15), 7610−7630.
(7) Mathiesen, J. K.; Quinson, J.; Blaseio, S.; Kjær, E. T.; Dworzak, A.; Cooper, S. R.; Pedersen, J. K.; Wang, B.; Bizzotto, F.; Schröder, J.; et al. Chemical Insights into the Formation of Colloidal Iridium Nanoparticles from In Situ X-ray Total Scattering: Influence of Precursors and Cations on the Reaction Pathway. *J. Am. Chem. Soc.* **2023**, *145* (3), 1769−1782.
(8) Carbone, M. R.; Kim, H. J.; Fernando, C.; Yoo, S.; Olds, D.; Joress, H.; DeCost, B.; Ravel, B.; Zhang, Y. G.; Maffettone, P. M. Flexible formulation of value for experiment interpretation and design. *Matter* **2024**, *7* (2), 685−696, DOI: 10.1016/j.matt.2023.11.012.
(9) Akkerman, Q. A.; Rainò, G.; Kovalenko, M. V.; Manna, L. Genesis, challenges and opportunities for colloidal lead halide perovskite nanocrystals. *Nat. Mater.* **2018**, *17* (5), 394−405.
(10) Lu, F.; Zhang, Y. G.; Zhang, L. H.; Su, D.; Zhuang, Z. C.; Liu, M. Z.; Chen, J. G. G.; Gang, O. L. Continuous Encodable Reshaping of Gold Nanocrystals through Facet Modulation. *J. Am. Chem. Soc.* **2025**, *147* (29), 25871−25882.
(11) Pearce, A. K.; Wilks, T. R.; Arno, M. C.; O'Reilly, R. K. Synthesis and applications of anisotropic nanoparticles with precisely defined dimensions. *Nat. Rev. Chem.* **2021**, *5* (1), 21−45.
(12) O'Brien, M. N.; Jones, M. R.; Mirkin, C. A. The nature and implications of uniformity in the hierarchical organization of nanomaterials. *Proc. Natl. Acad. Sci. U.S.A.* **2016**, *113* (42), 11717−11725.
(13) Sahi, S.; Magill, S.; Ma, L.; Xie, J.; Chen, W.; Jones, B.; Nygren, D. Wavelength-shifting properties of luminescence nanoparticles for high energy particle detection and specific physics process observation. *Sci. Rep.* **2018**, *8* (1), No. 10515.
(14) Nikolaev, P.; Hooper, D.; Webber, F.; Rao, R.; Decker, K.; Krein, M.; Poleski, J.; Barto, R.; Maruyama, B. Autonomy in materials research: a case study in carbon nanotube growth. *npj Comput. Mater.* **2016**, *2*, No. 16031, DOI: 10.1038/npjcompumats.2016.31.
(15) Tao, H.; Wu, T.; Aldeghi, M.; Wu, T. C.; Aspuru-Guzik, A.; Kumacheva, E. Nanoparticle synthesis assisted by machine learning. *Nat. Rev. Mater.* **2021**, *6* (8), 701−716.
(16) Szymanski, N. J.; Zeng, Y.; Huo, H.; Bartel, C. J.; Kim, H.; Ceder, G. Toward autonomous design and synthesis of novel inorganic materials. *Mater. Horiz.* **2021**, *8* (8), 2169−2198.
(17) Breen, C. P.; Nambiar, A. M.; Jamison, T. F.; Jensen, K. F. Ready, set, flow! Automated continuous synthesis and optimization. *Trends Chem.* **2021**, *3* (5), 373−386.
(18) Abolhasani, M.; Kumacheva, E. The rise of self-driving labs in chemical and materials sciences. *Nat. Synth.* **2023**, *2*, 483−492.
(19) Ferguson, A. L.; Brown, K. A. Data-driven design and autonomous experimentation in soft and biological materials engineering. *Annu. Rev. Chem. Biomol. Eng.* **2022**, *13*, 25−44.
(20) Wang, M.; Wang, T.; Cai, P.; Chen, X. Nanomaterials discovery and design through machine learning. *Small Methods* **2019**, *3* (5), No. 1900025.
(21) Li, Y.; Xia, L.; Fan, Y.; Wang, Q.; Hu, M. Recent advances in autonomous synthesis of materials. *ChemPhysMater* **2022**, *1* (2), 77−85.
(22) Vriza, A.; Chan, H.; Xu, J. Self-driving laboratory for polymer electronics. *Chem. Mater.* **2023**, *35* (8), 3046−3056.
(23) Tom, G.; Schmid, S. P.; Baird, S. G.; Cao, Y.; Darvish, K.; Hao, H.; Lo, S.; Pablo-García, S.; Rajaonson, E. M.; Skreta, M.; et al. Self-driving laboratories for chemistry and materials science. *Chem. Rev.* **2024**, *124* (16), 9633−9732.
(24) Stach, E.; DeCost, B.; Kusne, A. G.; Hattrick-Simpers, J.; Brown, K. A.; Reyes, K. G.; Schrier, J.; Billinge, S.; Buonassisi, T.; Foster, I.; et al. Autonomous experimentation systems for materials development: A community perspective. *Matter* **2021**, *4* (9), 2702−2726.
(25) Cao, B.; Adutwum, L. A.; Oliynyk, A. O.; Luber, E. J.; Olsen, B. C.; Mar, A.; Buriak, J. M. How to optimize materials and devices via design of experiments and machine learning: Demonstration using organic photovoltaics. *ACS Nano* **2018**, *12* (8), 7434−7444.
(26) Vikram, A.; Brudnak, K.; Zahid, A.; Shim, M.; Kenis, P. J. Accelerated screening of colloidal nanocrystals using artificial neural network-assisted autonomous flow reactor technology. *Nanoscale* **2021**, *13* (40), 17028−17039.
(27) Li, J.; Lim, K.; Yang, H.; Ren, Z.; Raghavan, S.; Chen, P.-Y.; Buonassisi, T.; Wang, X. AI applications through the whole life cycle of material discovery. *Matter* **2020**, *3* (2), 393−432.
(28) Patungwasa, W.; Hodak, J. H. pH tunable morphology of the gold nanoparticles produced by citrate reduction. *Mater. Chem. Phys.* **2008**, *108* (1), 45−54.
(29) Vikram, A.; Kumar, V.; Ramesh, U.; Balakrishnan, K.; Oh, N.; Deshpande, K.; Ewers, T.; Trefonas, P.; Shim, M.; Kenis, P. J. A millifluidic reactor system for multistep continuous synthesis of InP/ZnSeS nanoparticles. *ChemNanoMat* **2018**, *4* (9), 943−953.
(30) Politi, M.; Baum, F.; Vaddi, K.; Antonio, E.; Vasquez, J.; Bishop, B. P.; Peek, N.; Holmberg, V. C.; Pozzo, L. D. A high-throughput workflow for the synthesis of CdSe nanocrystals using a sonochemical materials acceleration platform. *Digital Discovery* **2023**, *2*, 1042−1057, DOI: 10.1039/D3DD00033H.
(31) Chan, E. M. Combinatorial approaches for developing upconverting nanomaterials: high-throughput screening, modeling, and applications. *Chem. Soc. Rev.* **2015**, *44* (6), 1653−1679.
(32) Mekki-Berrada, F.; Ren, Z.; Huang, T.; Wong, W. K.; Zheng, F.; Xie, J.; Tian, I. P. S.; Jayavelu, S.; Mahfoud, Z.; Bash, D.; et al. Two-step machine learning enables optimized nanoparticle synthesis. *npj Comput. Mater.* **2021**, *7* (1), No. 55.
(33) Xie, Y.; Zhang, C.; Hu, X.; Zhang, C.; Kelley, S. P.; Atwood, J. L.; Lin, J. Machine learning assisted synthesis of metal−organic nanocapsules. *J. Am. Chem. Soc.* **2020**, *142* (3), 1475−1481.
(34) Gulevich, D.; Nabiev, I.; Samokhvalov, P. Machine learning−assisted colloidal synthesis: A review. *Mater. Today Chem.* **2024**, *35*, No. 101837.
(35) Masson, J.-F.; Biggins, J. S.; Ringe, E. Machine learning for nanoplasmonics. *Nat. Nanotechnol.* **2023**, *18* (2), 111−123.
(36) Chen, X.; Lv, H. Intelligent control of nanoparticle synthesis on microfluidic chips with machine learning. *NPG Asia Mater.* **2022**, *14* (1), No. 69.
(37) Zhao, H.; Chen, W.; Huang, H.; Sun, Z.; Chen, Z.; Wu, L.; Zhang, B.; Lai, F.; Wang, Z.; Adam, M. L.; et al. A robotic platform for the synthesis of colloidal nanocrystals. *Nat. Synth.* **2023**, *2* (6), 505−514.
(38) Salley, D.; Keenan, G.; Grizou, J.; Sharma, A.; Martín, S.; Cronin, L. A nanomaterials discovery robot for the Darwinian evolution of shape programmable gold nanoparticles. *Nat. Commun.* **2020**, *11* (1), No. 2771.
(39) Coley, C. W.; Thomas, D. A., III; Lummiss, J. A.; Jaworski, J. N.; Breen, C. P.; Schultz, V.; Hart, T.; Fishman, J. S.; Rogers, L.; Gao, H.; et al. A robotic platform for flow synthesis of organic compounds informed by AI planning. *Science* **2019**, *365* (6453), No. eaax1566.
(40) Fong, A. Y.; Pellouchoud, L.; Davidson, M.; Walroth, R. C.; Church, C.; Tcareva, E.; Wu, L.; Peterson, K.; Meredig, B.; Tassone, C. J. Utilization of machine learning to accelerate colloidal synthesis and discovery. *J. Chem. Phys.* **2021**, *154* (22), No. 224201, DOI: 10.1063/5.0047385.
(41) Tao, H.; Wu, T.; Kheiri, S.; Aldeghi, M.; Aspuru-Guzik, A.; Kumacheva, E. Self-driving platform for metal nanoparticle synthesis: combining microfluidics and machine learning. *Adv. Funct. Mater.* **2021**, *31* (51), No. 2106725.
(42) Volk, A. A.; Epps, R. W.; Yonemoto, D. T.; Masters, B. S.; Castellano, F. N.; Reyes, K. G.; Abolhasani, M. AlphaFlow: autonomous discovery and optimization of multi-step chemistry

https://doi.org/10.1021/jacs.5c03875
J. Am. Chem. Soc. XXXX, XXX, XXX−XXX

using a self-driven fluidic lab guided by reinforcement learning. *Nat. Commun.* **2023**, *14* (1), No. 1403.
(43) Epps, R. W.; Delgado-Licona, F.; Yang, H.; Kim, T.; Volk, A. A.; Han, S.; Jun, S.; Abolhasani, M. Accelerated Multi-Stage Synthesis of Indium Phosphide Quantum Dots in Modular Flow Reactors. *Adv. Mater. Technol.* **2023**, *8* (4), No. 2201845.
(44) Levenstein, M. A.; Wayment, L.; Scott, C. D.; Lunt, R.; Flandrin, P.-B.; Day, S. J.; Tang, C. C.; Wilson, C. C.; Meldrum, F. C.; Kapur, N.; Robertson, K. Dynamic crystallization pathways of polymorphic pharmaceuticals revealed in segmented flow with inline powder X-ray diffraction. *Anal. Chem.* **2020**, *92* (11), 7754−7761.
(45) Jackson, C.; Robertson, K.; Sechenyh, V.; Chamberlain, T. W.; Bourne, R. A.; Lester, E. Self-optimizing continuous-flow hydrothermal reactor for nanoparticle synthesis. *React. Chem. Eng.* **2025**, *10*, 511−514, DOI: 10.1039/d4re00339j.
(46) Rakita, Y.; O'Nolan, D.; McAuliffe, R. D.; Veith, G. M.; Chupas, P. J.; Billinge, S. J.; Chapman, K. W. Active reaction control of Cu redox state based on real-time feedback from in situ synchrotron measurements. *J. Am. Chem. Soc.* **2020**, *142* (44), 18758−18762.
(47) Pithan, L.; Starostin, V.; Mareček, D.; Petersdorf, L.; Völter, C.; Munteanu, V.; Jankowski, M.; Konovalov, O.; Gerlach, A.; Hinderhofer, A.; et al. Closing the loop: autonomous experiments enabled by machine-learning-based online data analysis in synchrotron beamline environments. *J. Synchrotron Radiat.* **2023**, *30* (6), 1064−1075.
(48) Li, T.; Senesi, A. J.; Lee, B. Small Angle X-ray Scattering for Nanoparticle Research. *Chem. Rev.* **2016**, *116* (18), 11128−11180.
(49) Turkevich, J.; Stevenson, P. C.; Hillier, J. A Study of the Nucleation and Growth Processes in the Synthesis of Colloidal Gold. *Discuss. Faraday Soc.* **1951**, *11* (11), 55−75.
(50) Dong, J.; Carpinone, P. L.; Pyrgiotakis, G.; Demokritou, P.; Moudgil, B. M. Synthesis of precision gold nanoparticles using Turkevich method. *KONA Powder Part. J.* **2020**, *37*, 224−232.
(51) Wuithschick, M.; Birnbaum, A.; Witte, S.; Sztucki, M.; Vainio, U.; Pinna, N.; Rademann, K.; Emmerling, F.; Kraehnert, R.; Polte, J. Turkevich in new robes: key questions answered for the most common gold nanoparticle synthesis. *ACS Nano* **2015**, *9* (7), 7052−7071.
(52) Link, S.; El-Sayed, M. A. Size and temperature dependence of the plasmon absorption of colloidal gold nanoparticles. *J. Phys. Chem. B* **1999**, *103* (21), 4212−4217.
(53) Haiss, W.; Thanh, N. T. K.; Aveyard, J.; Fernig, D. G. Determination of size and concentration of gold nanoparticles from UV-Vis spectra. *Anal. Chem.* **2007**, *79* (11), 4215−4221.
(54) Khlebtsov, N. G. Determination of size and concentration of gold nanoparticles from extinction spectra. *Anal. Chem.* **2008**, *80* (17), 6620−6625.
(55) Kreibig, U.; Vollmer, M. *Optical Properties of Metal Clusters*; Springer: Berlin ; New York, 1995; p 532.
(56) Kelly, K. L.; Coronado, E.; Zhao, L. L.; Schatz, G. C. The optical properties of metal nanoparticles: The influence of size, shape, and dielectric environment. *J. Phys. Chem. B* **2003**, *107* (3), 668−677.
(57) Tyagi, H.; Kushwaha, A.; Kumar, A.; Aslam, M. A facile pH controlled citrate-based reduction method for gold nanoparticle synthesis at room temperature. *Nanoscale Res. Lett.* **2016**, *11*, No. 362.
(58) Chow, M.; Zukoski, C. Gold sol formation mechanisms: role of colloidal stability. *J. Colloid Interface Sci.* **1994**, *165* (1), 97−109.
(59) Frens, G. Controlled nucleation for the regulation of the particle size in monodisperse gold suspensions. *Nat. Phys. Sci.* **1973**, *241* (105), 20−22.

https://doi.org/10.1021/jacs.5c03875
J. Am. Chem. Soc. XXXX, XXX, XXX−XXX